



Cite this: *RSC Adv.*, 2019, 9, 22764

TiO₂/Fe₂O₃ heterostructures with enhanced photocatalytic reduction of Cr(vi) under visible light irradiation†

Qiufeng Mei,^a Feiyan Zhang,^a Ning Wang,^a Yun Yang,^b Ronglan Wu^b ^{*a} and Wei Wang^c ^{*c}

We report a study on the synthesis of TiO₂/Fe₂O₃ (TF) nanocomposites and their photocatalytic performance under visible-light irradiation. The characterization of structure and morphology shows that hematite Fe₂O₃ was deposited on anatase TiO₂ nanoparticles with particle sizes in the range of 20–100 nm. In contrast to pure TiO₂ and pure Fe₂O₃, the nanocomposites exhibited remarkable photocatalytic activity. For example, the photoreduction efficiency of TF0.5 reaches 100% for a 100 ppm Cr(vi) solution within 160 minutes. The photochemical properties were studied by various methods. Finally, we conclude that the excellent performance of the photocatalysts is mainly attributed to two aspects: the enhanced absorption of visible light and the synergistic effect of an internal electric field at the heterojunction and citric acid for promoting the separation of electron–hole pairs.

Received 11th May 2019

Accepted 13th July 2019

DOI: 10.1039/c9ra03531a

rsc.li/rsc-advances

Introduction

Photocatalysis, in which an artificial photosynthetic system is set up for the conversion of solar energy to chemical energy, has been of great significance in environmental conservation and energy utilization.^{1,2} Over the last few decades, research in the area has been focusing on improving photochemical quantum yields. With this objective, various photocatalysts, especially semiconductor photocatalysts (TiO₂,^{3,4} Fe₂O₃,^{5,6} CuS,⁷ MoS₂,^{8,9} g-C₃N₄,¹⁰ Ag₂O,¹¹ WO₃,¹² etc.) have received great attention. Among these photocatalysts, TiO₂ and its composites exhibit great potential due to their unique features (*i.e.* non-toxicity, low cost, high chemical inertness and photostability^{13–15}). However, there are two intrinsic defects limiting the practical application of TiO₂: (i) its wide band gap energy (3.0–3.2 eV) restricts its response to visible light; (ii) the rapid recombination of photogenerated electron–hole pairs, which leads to the decrease of its photocatalytic activity.¹⁵ Therefore, much effort has been devoted to solving these problems.

One solution to overcome the defects is to construct heterojunction photocatalysts. Due to the features of the heterojunction, the spatial separation of electron–hole pairs is

naturally in place,¹⁶ which prevents the rapid recombination of photogenerated electron–hole pairs. In spite of the above-mentioned advantage, heterojunction photocatalysts can extend the light responsive range through coupling with narrow band gap semiconductors.^{17,18} In order to construct a suitable TiO₂-based heterojunction photocatalyst, the matching of energy levels between the two components is crucial, that is, the conduction band edge of the narrow band gap semiconductor is higher than that of TiO₂.¹⁹ Fe₂O₃, as a highly active photocatalyst with a band gap of 2.2 eV, seems to be a good choice except it has a lower conduction band edge.^{20–22} However, the Fermi level (*E_F*) of Fe₂O₃ is lower than that of TiO₂.²³ Therefore, band bending may occur so that the conduction band edge of Fe₂O₃ is higher than that of TiO₂ when their Fermi levels are equalized.²⁴ In addition, the internal electric field will also be constructed by Fermi level alignment, which further promotes the separation of electron–hole pairs. In short, it is promising for TiO₂ coupled with Fe₂O₃ to be a desired heterojunction photocatalyst.

In this study, we have developed a facile synthetic strategy (Scheme 1) to fabricate sheet-like TiO₂/Fe₂O₃ nanocomposites for photoreduction Cr(vi). Specifically, TiO₂ nanoparticles were synthesised by a solvothermal approach in the mixed solution of HF and *N,N*-dimethyl formamide (DMF). Iron ions particularly adsorb on the negatively charged TiO₂ nanoparticles by electrostatic interaction. As a result, Fe₂O₃ was deposited on the surface of TiO₂ by hydrothermal method. After calcination, TiO₂/Fe₂O₃ nanocomposites formed. The as-prepared TiO₂/Fe₂O₃ composites as a photocatalyst exhibited excellent performance for photoreduction of Cr(vi).

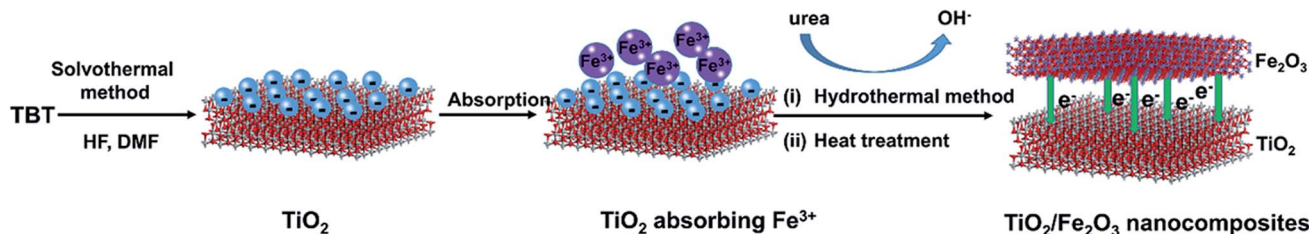
^aKey Laboratory of Oil & Gas Fine Chemicals, College of Chemistry and Chemical Engineering of Xinjiang University, Urumqi 830046, China. E-mail: wuronglan@163.com

^bNanomaterials and Chemistry Key Laboratory, Wenzhou University, Wenzhou 325027, China

^cDepartment of Chemistry and Center for Pharmacy, University of Bergen, Bergen 5020, Norway. E-mail: wei.wang@uib.no

† Electronic supplementary information (ESI) available. See DOI: 10.1039/c9ra03531a





Scheme 1 Schematic diagram of fabricating $\text{TiO}_2/\text{Fe}_2\text{O}_3$ nanocomposites.

Experimental sections

Chemicals

Tetrabutyl titanate (TBT, 99.0%), *N,N*-dimethyl formamide (DMF, 99.5%), hydrofluoric acid (HF, 40%, w/w), ferric sulfate ($\text{Fe}_2(\text{SO}_4)_3$, 99.0%), urea (CON_2H_4 , 99.0%), potassium dichromate ($\text{K}_2\text{Cr}_2\text{O}_7$, 99.0%) and citric acid were purchased from Zhiyuan Chemical Reagent Co., Ltd (Tianjin, China), and used as received. Deionized water was used in all experiments.

Synthesis of TiO_2 nanoparticles

We modified a hydrothermal method reported previously to synthesize TiO_2 nanoparticles.^{25,26} TBT (5.0 mL) was firstly dissolved in 5.0 mL of DMF and then mixed with 1.0 mL of HF to form white suspension, which was subsequently transferred into a 25 mL Teflon-lined autoclave and reacted for 24 hours at 180 °C. A white product was collected and washed with deionized water until the pH of the suspension is about 7.0, and then washed with ethanol for several times. The product was dried at 80 °C for 12 hours, and afterwards annealed at 400 °C in air for 2 hours to obtain TiO_2 .

Preparation of $\text{TiO}_2/\text{Fe}_2\text{O}_3$ nanocomposites

$\text{Fe}_2(\text{SO}_4)_3$ (0.2 g, 0.5 mmol) was dissolved in 70 mL of deionized water, then 0.5 g of as-prepared TiO_2 was added to the solution and mixed under vigorous stirring for 12 hours. Following this, 0.18 g of urea (the molar ratio of urea to $\text{Fe}_2(\text{SO}_4)_3$ is 6 : 1) was added into the suspension, which was then transferred into a 100 mL Teflon-lined autoclave and maintained at 160 °C for 5 hours. The obtained precipitates were washed several times with water and ethanol and dried at 80 °C for 8 hours. The dried powder was calcined in a tube furnace at 500 °C for 2 hours with a heating rate of 5 °C min^{-1} in Ar atmosphere. After cooling down to room temperature, the light red $\text{TiO}_2/\text{Fe}_2\text{O}_3$ powder was obtained and named as TF0.5. In comparison, pure Fe_2O_3 and a series of products with different content of Fe_2O_3 were prepared under the same conditions. The products are noted as TF x where x represents the amount of $\text{Fe}_2(\text{SO}_4)_3$ in mmol. For example, TF2.0 means that the amount of $\text{Fe}_2(\text{SO}_4)_3$ is 2.0 mmol in the reaction.

Characterization of $\text{TiO}_2/\text{Fe}_2\text{O}_3$ nanocomposites

The morphology of $\text{TiO}_2/\text{Fe}_2\text{O}_3$ nanocomposites was observed by scanning electron microscopy (SEM, LEO 1430VP, Germany),

transmission electron microscopy (TEM, JEM2100F, Japan). Scanning transmission electron microscopy (STEM) images, selected area electron diffraction (SAED) patterns and high-angle annular dark-field scanning transmission electron microscopy (HAADF-STEM) images were obtained on a high-resolution transmission electron microscopy (HR-TEM, FEI Tecnai G2 F20, America) with HAADF detector operator at 300 kV. BET specific surface area was measured at 77.5 K on a nitrogen adsorption apparatus (Micromeritics ASAP 2460, America) after samples were vacuum-dried at 180 °C overnight. The crystal structure of the composites was confirmed by X-ray diffractometer (XRD, D8 Focus-ADVANCE, Germany Bruker) with Cu source radiation ($\lambda = 0.15418$ nm). X-ray photoelectron spectroscopy (XPS, ESCALAB 250Xi, American Thermo Fisher Scientific) equipped with Al source radiation (1486.6 eV) was used to analyse bonding information of the composites. The UV-vis diffuse reflectance (UV-vis DRS) spectra of the composites over a range of 200–800 nm were tested by a U-3010 spectrophotometer using BaSO_4 as a standard reference. The photoluminescence (PL) spectra of the composites were obtained by using the fluorescence spectrophotometer (F-4500 FL) with an excitation wavelength of 325 nm. Under visible light irradiation ($\lambda > 420$ nm), the electron spin response (ESR) signals of superoxide radicals spin-trapped by spin-trapped reagent 5,5-dimethyl-L-pyrroline *N*-oxide (DMPO) were investigated on a Bruker EMXmicro-6/1/P/L (Karlsruhe, Germany) spectrometer.

Photocatalytic reduction of $\text{Cr}(\text{vi})$

The photocatalytic perform of $\text{TiO}_2/\text{Fe}_2\text{O}_3$ nanocomposites was investigated by the reduction of $\text{Cr}(\text{vi})$ in acid conditions with visible-light irradiation. The photocatalytic measurements were carried out in the photocatalytic reaction apparatus (XPA-7, Xujiang). Typically, 50 mL of 100 ppm $\text{K}_2\text{Cr}_2\text{O}_7$ solution and 1 mL of 100 mg mL^{-1} citric acid solution were mixed in a quartz tube, and then 50 mg of photocatalyst was dispersed in the solution. The mixture was treated in an ultrasonic bath for 5 minutes. The suspension was stirred at 900 rpm for 40 minutes in dark to reach equilibrium of adsorption. Subsequently, the suspension was irradiated by a 500 W Au halide lamp equipped with cutoff filters ($\lambda > 420$ nm). A sample of 2 mL suspension was collected at a 20 minute interval. Then the collected suspension was filtered using 0.45 μm filter membrane to remove photocatalysts. The concentration of $\text{Cr}(\text{vi})$ was



determined by UV-vis spectrometer (UV-2550, Shimadzu) after the filtrate was treated with diphenylcarbonylhydrazine.

Photoelectrochemical measurements

The transient photocurrent responses and electrochemical impedance spectroscopy (EIS) measurements of the samples were operated on a CHI660E electrochemical workstation equipped with a standard three-electrode system. A Pt wire, an Ag/AgCl electrode and 0.5 M Na₂SO₄ solution (pH = 6.8) were used as the counter electrode, the reference electrode and the electrolyte solution, respectively. The preparation of the working electrode is as follows. The photocatalyst (20 mg) was ultrasonically dispersed into 0.5 mL of deionized water to obtain the slurry. The slurry (200 μ L) was evenly spread on a fluorine-doped tin oxide (FTO) glass and dried at room temperature, subsequently dried at 120 $^{\circ}$ C for 12 hours in vacuum. The area of samples daubed on the FTO glass is 1.0 cm². A 300 W xenon lamp (PL-X300D) equipped with a cutoff filter ($\lambda > 420$ nm) was used as a source of visible light.

Results and discussion

Morphologies and structures of TiO₂/Fe₂O₃ nanocomposites

The TEM images show that pure TiO₂ exhibits irregular a sheet-like structure with the size of 20–100 nm (Fig. 1a) and pure Fe₂O₃ exhibits a flower-like structure with the size of about

500 nm (Fig. 1c). However, the TEM images of TF nanocomposites including TF0.5 (Fig. 1b), TF0.1 and TF2.0 (Fig. S1†) show only the sheet-like structure rather than the flower-like structure. This result could be understood as TiO₂ adsorbing iron ions restricts its aggregation and growth, and additionally urea solution slowly releases OH[−] at high temperature, which slows down the hydrolysis rate of Fe³⁺. In addition, TiO₂ nanoparticles are getting more and more agglomerated with the increase of Fe₂O₃ on TiO₂ sheets from TF0.1 to TF2.0, which can be understood by the electrostatic interaction between negatively charged TiO₂ and positively charged Fe₂O₃. The quantitative characterization of the surface charge was measured by zeta potential (Table S1 in ESI†). The zeta potential of pure TiO₂, TF0.1, TF0.2, TF0.5, TF1.0, TF2.0 and pure Fe₂O₃ are −5.96 mV, 5.07 mV, 9.76 mV, 12.18 mV, 18.68 mV, 17.92 mV and 7.98 mV, respectively. Clearly, the surface charge increases with the amount of positively charged Fe₂O₃. The positive charge on the TF composites indicates that the surface of the composites is covered by Fe₂O₃ nanoparticles. The SEM image (Fig. S2†) further reveals that the aggregation of TF0.5 nanocomposite is composed of many stacked nanoparticles of smaller size.

Fig. 1 (d–f) present N₂ adsorption–desorption isotherm and pore size distribution of TiO₂, TF0.5 and Fe₂O₃. Obvious, the typical hysteresis loops indicate the capillary condensation associated with pores between the nanoparticles and suggest that TiO₂, TF0.5 and Fe₂O₃ are mesoporous materials. Their

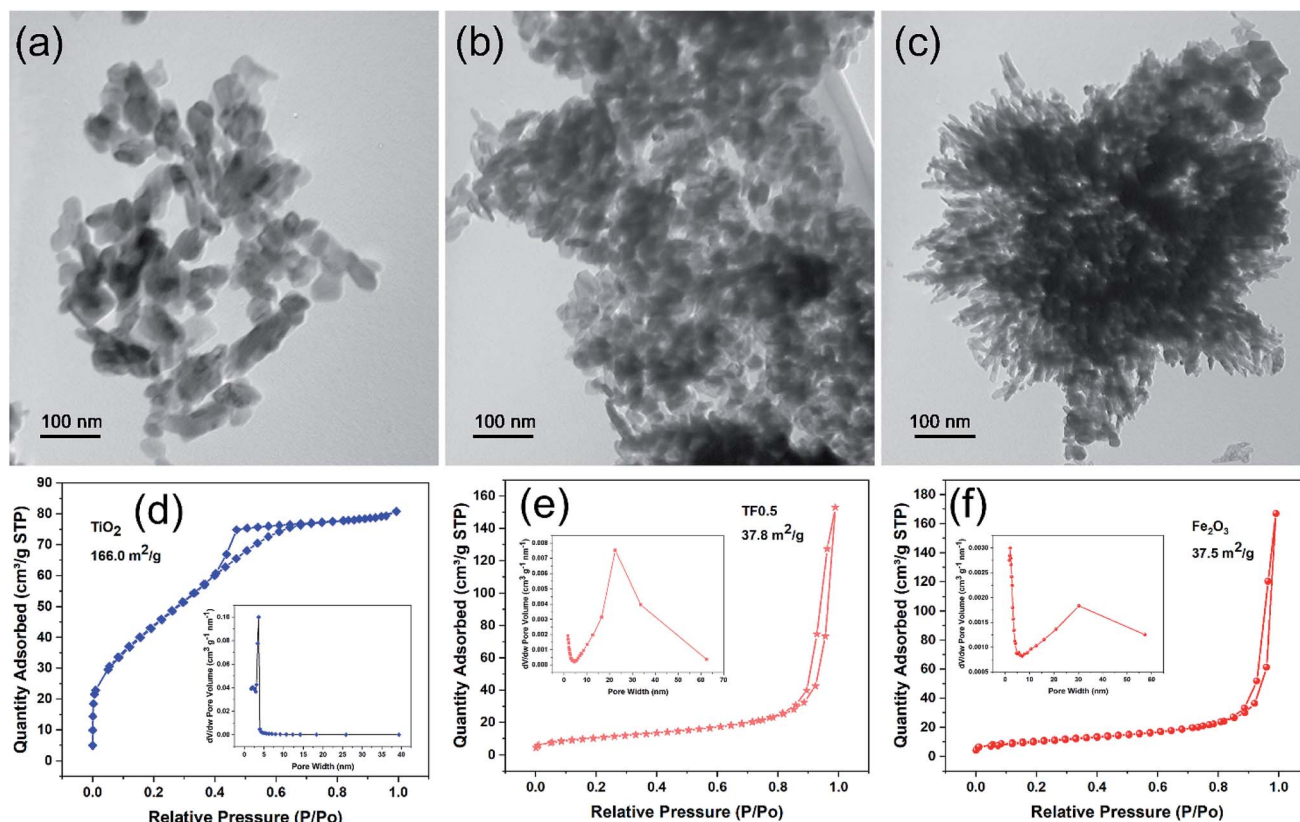


Fig. 1 (a–c) The TEM images of TiO₂, TF0.5 and Fe₂O₃, and their corresponding (d–f) N₂ adsorption–desorption isotherm and pore size distribution curves.



average pore sizes by BJH desorption are 2.97, 24.90 and 27.98 nm, respectively. The corresponding BET surface area are calculated to be 166.0, 37.8 and 37.5 m² g⁻¹, respectively. These results show that pure TiO₂ has the largest specific surface area and the smallest pore, while TF0.5 and Fe₂O₃ have similar specific surface area and pore size. It can be proved that TiO₂ and Fe₂O₃ have strong interface attraction and gather together, which is consistent with the TEM results.

The HRTEM images and fast Fourier transform (FFT) patterns (Fig. 2) were used to resolve the lattice structures of TiO₂, TF0.5 and Fe₂O₃ and the difference in morphology for Fe₂O₃ deposited on the surface of TiO₂. Multiple crystal particle with different orientations in the HRTEM image of TiO₂ (Fig. 2a) proves that the prepared TiO₂ is polycrystalline, which agrees with the result of the FFT pattern (Fig. 2d). The FFT pattern of Fe₂O₃ in Fig. 2f demonstrates its single crystal structure sitting against a plane perpendicular to the [001] zone axis. As shown in Fig. 2c, the lattice fringe spacing of 0.25 nm can be indexed to six side facets of {110} of hexagonal Fe₂O₃.²⁷ Fig. 2e and S3† show that the structure of TF0.5 is polycrystalline, which is consistent with the observation in Fig. 2b, as an area with several crystalline domains is observed, including the {101} facet of anatase TiO₂ (*d* = 0.35 nm)²⁸ and the {104} facet of hematite Fe₂O₃ (*d* = 0.27 nm). This result illustrates that Fe₂O₃ was successfully deposited on the surface of TiO₂ and was in direct contact with each other.

The crystal structures of TiO₂ synthesized at 180 °C, TF0.5 and Fe₂O₃ have been confirmed by XRD (Fig. 3a). The diffraction peaks of TiO₂ and Fe₂O₃ could be indexed to anatase phase TiO₂ (JCPDS no. 21-1272) and hematite phase Fe₂O₃ (JCPDS no. 33-0664), and the phase is pure. Compared to the diffraction peaks of TiO₂, two new peaks at 2θ = 33.2° and 35.8° appear on the XRD pattern of TF0.5 nanocomposites, corresponding to the (104) and (110) planes of hematite Fe₂O₃, respectively. The increase of Fe₂O₃ content from TF0.1 to TF2.0 leads to the intensity enhancement of two characteristic peaks of hematite Fe₂O₃ on the XRD patterns (Fig. 3b). Moreover, the reference intensity ratio (RIR) method^{29,30} is used to analyze the weight fraction of the two crystal phases in the composite. The weight

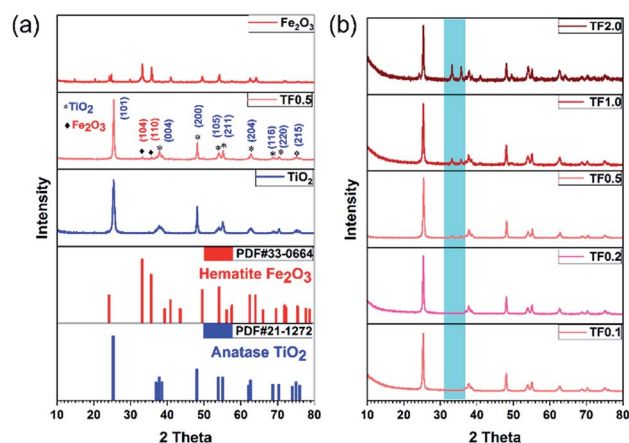


Fig. 3 (a) XRD patterns of TiO₂, TF0.5 and Fe₂O₃. (b) Comparison of XRD patterns of TF0.1, TF0.2, TF0.5, TF1.0 and TF2.0.

fractions of hematite Fe₂O₃ from TF0.1 to TF2.0 are 4.5%, 5.6%, 11.0%, 19.7% and 38.9%, respectively (also see Table S1†)

TEM and element mapping images (Fig. 4a–e) were used to investigate the microstructure and the element distribution of the as-prepared photocatalysts. The maps of HAADF (Fig. 4b), Ti (Fig. 4c), Fe (Fig. 4d) and O (Fig. 4e) match very well with the silhouette of black nanoparticles shown in Fig. 4a, which provides a clear evidence that Fe₂O₃ is homogeneously deposited on TiO₂. Evidently, the mapping profile of Fe is distinct from those of Ti and O in distribution, as a result of low content of Fe₂O₃ in TF0.5. The major elemental compositions of TF0.5 are further revealed by energy dispersive spectroscopy (EDS). All elements (Ti, Fe, C and O) were detected in TF0.5. As shown in Fig. 4f, the main signals of O, C, Ti and Fe elements are observed in the EDS spectrum of TF0.5, and the corresponding weight fractions are 37.0%, 32.3%, 30.3% and 0.4%, respectively.

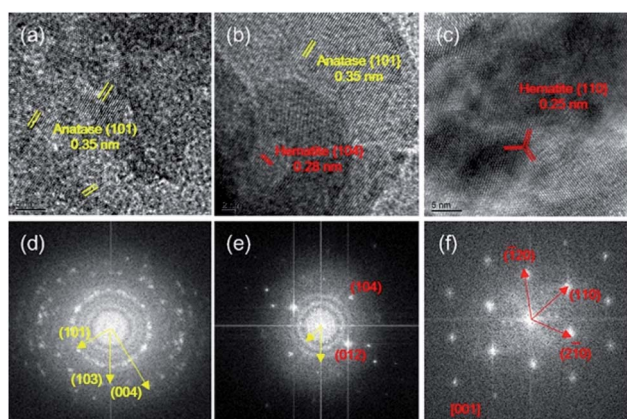


Fig. 2 HRTEM images of (a) TiO₂, (b) TF0.5 and (c) Fe₂O₃, and their corresponding fast Fourier transform (FFT) patterns (d–f).

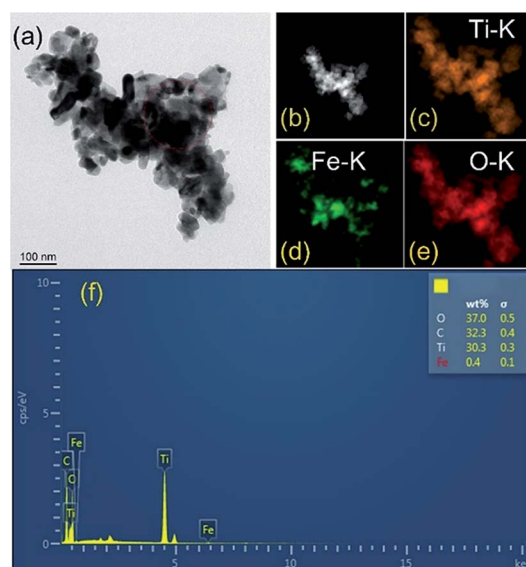


Fig. 4 (a) The TEM image, (b) HAADF-STEM image, (c) Ti, (d) Fe and (e) O elements mapping images and (f) EDS spectrum of TF0.5.



The element composition and chemical states on the surface of pure TiO_2 and TF0.5 nanocomposites can be determined by XPS. The XPS survey spectra (Fig. 5a) of pure TiO_2 and TF0.5 shows the presence of Ti, O, C and F elements on their surfaces; while, Fe element exists only in TF0.5 in addition to the four elements. In the high-resolution Fe 2p spectrum (Fig. 5b) of TF0.5, two binding energy peaks are found at 711.0 and 724.5 eV, corresponding to $\text{Fe } 2p_{3/2}$ and $\text{Fe } 2p_{1/2}$, respectively. The difference of two peaks (ΔBE) is 13.5 eV, which is the characteristics of Fe(III) .^{31,32} In the high-resolution Ti 2p spectra (Fig. 5c) of TF0.5 and TiO_2 , the ΔBE of $\text{Ti } 2p_{3/2}$ and $\text{Ti } 2p_{1/2}$ is 5.6 eV, which features Ti(IV) .^{33–35} Moreover, the two peaks of binding energy of $\text{Ti } 2p_{1/2}$ and $\text{Ti } 2p_{3/2}$ of TF0.5 are 464.3 eV and 458.7 eV, respectively, which are lower than those of pure TiO_2 . This decrease of ΔBE for Ti(IV) may provide an indirect evidence of forming the Ti–O–Fe bond since the internal electric field promotes the electron transfer from Fe_2O_3 to TiO_2 .^{33,36} Two peaks of O 1s spectrum (Fig. 5d) of TF0.5 appear at 530.0 eV and 531.6 eV, corresponding to lattice oxygen and O–H bond,³⁷ respectively. However, the binding energy of O–H bond in TF0.5 is lower than that in TiO_2 , which further confirms the formation of the Ti–O–Fe bond.

Light absorption of photocatalysts

The band energy structures of semiconducting materials are key factors to their optoelectronic properties.³⁸ Therefore, it is crucial to study light absorption ability to probe the band structure of the materials before photocatalytic experiments. The simplest method for this purpose is to measure its optical absorption spectrum. UV-vis diffuse reflectance spectra (UV-vis DRS) were obtained in Fig. 6a. Pure Fe_2O_3 and its composites with different amount of Fe_2O_3 exhibit nearly same absorption edge. Pure TiO_2 shows almost no absorption in visible region;

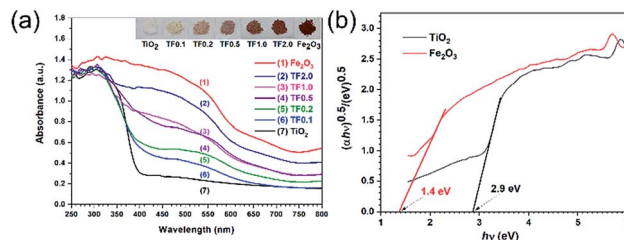


Fig. 6 (a) UV-vis diffuse reflectance spectra and (b) plots of $(\alpha h\nu)^{0.5}$ versus photon energy for calculation of bandgap energies of TiO_2 and Fe_2O_3 .

while, the $\text{TiO}_2/\text{Fe}_2\text{O}_3$ nanocomposites showed increase in absorption with the amount of Fe_2O_3 in the composites, implying that the response of the composites to visible light can be ascribed to the light absorption of Fe_2O_3 .

The optical band gap energy is determined by the Tauc equation:^{39–43}

$$(\alpha h\nu)^{1/n} = A(h\nu - E_g)$$

where A is proportionality constant; h is Planck's constant; ν is the photon's frequency; E_g is energy of optical band gap; α is absorption coefficient; the value of the exponent represents the character of the electronic transition, whether direct or indirect: n is 0.5 for direct band gap materials or 2 for indirect band gap materials. The bandgap is estimated from the intercept of the extrapolated linear fit to the Tauc plot.³⁸ Both TiO_2 and Fe_2O_3 is well known to have an indirect band gap,^{44–46} so we plotted $(\alpha h\nu)^{0.5}$ versus photon energy to calculate the bandgap energies of TiO_2 and Fe_2O_3 (Fig. 6b). The intercepts of the Tauc plot give the optical band gaps energies, which are 2.9, and 1.4 eV for TiO_2 and Fe_2O_3 , respectively. Based on the results, the $\text{TiO}_2/\text{Fe}_2\text{O}_3$ nanocomposites with a narrow band gap are expected to exhibit visible-light driven photocatalytic activity.

Photoreduction Cr(vi) of as-prepared photocatalysts

Photocatalytic reduction of Cr(vi) was carried out to compare the photocatalytic activity for the as-prepared photocatalysts under visible light irradiation (Fig. 7a). During the dark adsorption process of 40 minutes, there was no decrease in the concentration of Cr(vi) , which indicated that there was no adsorption of Cr(vi) on the nanocomposites and no chemical reaction for

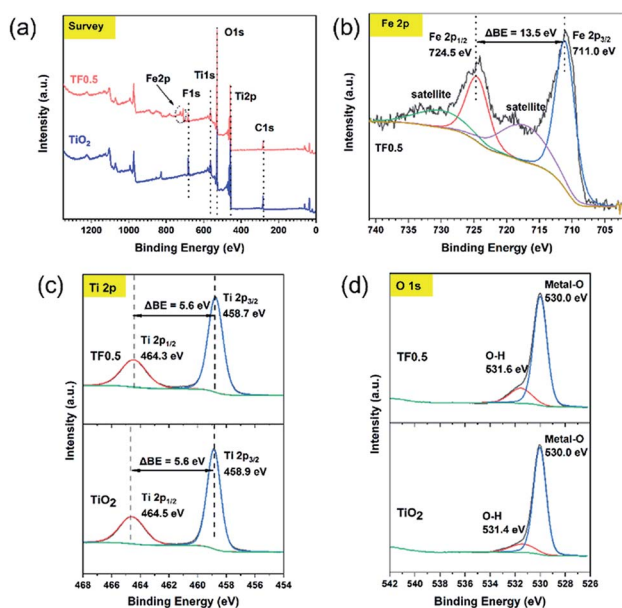


Fig. 5 (a) The survey spectra of TiO_2 and TF0.5, and the high-resolution XPS spectra of (b) Fe 2p, (c) Ti 2p and (d) O 1s.

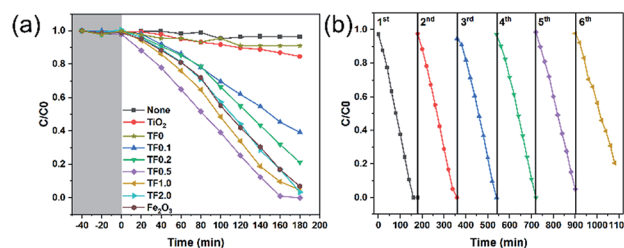


Fig. 7 (a) Photocatalytic performances of TiO_2 , TF0, TF0.1, TF0.2, TF0.5, TF1.0, TF2.0 and Fe_2O_3 for reduction of Cr(vi) under visible light irradiation. (b) Cyclic photoreduction Cr(vi) experiments of TF0.5.



Cr(VI). Therefore, the subsequent decrease of Cr(VI) concentration is not affected by adsorption and redox reaction, while, only depends on the photocatalytic reduction. Based on the trend of C/C_0 curves, we find that TF0.5 has the highest photocatalytic efficiency, and the reduction efficiency of Cr(VI) achieves 100% within 160 minutes. Cyclic photoreduction of Cr(VI) for TF0.5 has been conducted to investigate its photochemical stability. After five cycles of photoreduction, the TF0.5 photocatalyst did not exhibit any significant loss of photocatalytic activity (Fig. 7b). The crystal structure of TF0.5 remained the same after cyclic experiments (see the XRD patterns in Fig. S4†). But there was a significant drop in the sixth cycle, which was attributed to the loss of Fe_2O_3 . This drop in photocatalytic activity is understood by photocorrosion, where a part of Fe_2O_3 has been reduced to Fe(II) in the process of photoreduction Cr(VI).^{47,48}

Electronic and optical properties of photocatalysts

To investigate the photoelectrochemical properties, the electrochemical impedance spectra (EIS) of photocatalysts and the transient photocurrent responses of TiO_2 , TF0.5 and Fe_2O_3 are given in Fig. 8. As shown in Fig. 8a, the alternating cycles of visible light irradiation and dark process of photocatalysts are at a fixed interval of 30 seconds. The photocurrent density of the photocatalysts under visible-light irradiation obviously increases in comparison to the dark current density. The photocurrent density of a photocatalyst is correlated to its photocatalytic ability as higher photocurrent density indicates high separation efficiency of photogenerated carriers.⁴⁹ TF0.5 shows enhanced photocurrent density as about $1.4 \mu\text{A cm}^{-2}$, indicating its enhanced charge separation efficiency. In the recycles of turning on and off the light, the current density of TF0.5 continuously decrease to $1.3 \mu\text{A cm}^{-2}$, which is ascribed to the loss Fe_2O_3 as demonstrated in the photocatalytic recycle experiment. Fig. 8b shows electrochemical impedance spectra of TiO_2 , TF0.5 and Fe_2O_3 . All spectra display a circular arc at a frequency of 10^{-2} to 10^5 Hz, indicating the charge transfer

process. The radius of the arc can be explained as the resistance of charge transfer.⁵⁰ TF0.5 has smaller radius than other photocatalysts, meaning an easier charge transfer between TiO_2 and Fe_2O_3 .

Efficient separation of electron-hole pairs determines the photocatalytic activity of photocatalysts. The recombination of electron-hole pairs lead to fluorescence emission, so photoluminescence (PL) spectroscopy is an important means for probing the extent of charge separation as the lower PL intensity of the catalyst indicates the lower recombination rate and higher photocatalytic activity.^{51,52} Fig. 8c shows the emission intensity of PL for the as-prepared photocatalysts with an excitation wavelength of 325 nm. The pure TiO_2 show a high PL intensity at 415 nm and 470 nm but the PL intensity decreases when TiO_2 forms composites with Fe_2O_3 , demonstrating the efficient charge separation of the composites. The PL intensity of TF0.5 is the lowest, which is in accord with its high photocatalytic activity. In short, the results of the PL spectra, the transient photocurrent responses and the EIS spectra of the photocatalysts are in consistence with the photocatalytic performance.

Photocatalytic mechanism

The band structures of TiO_2 and Fe_2O_3 were obtained by the Mott-Schottky plots (Fig. S5†). TiO_2 shows a positive slope, indicating the n-type semiconductor characteristic of TiO_2 ; on the contrary, Fe_2O_3 shows a negative slope, indicating the p-type semiconductor characteristic of Fe_2O_3 . The flat band position of semiconductors is the intercept on the x axis of the extrapolated linear fit of the Mott-Schottky plot and is close to their conduction band (CB) position.^{53,54} Hence, the estimated CB positions of TiO_2 and Fe_2O_3 are -0.84 and -0.32 V, respectively (vs. Ag/AgCl, pH = 6.8). These two potentials are converted to -0.22 and $+0.30$ V (vs. NHE, pH = 0). Combined with the bandgap of TiO_2 (2.9 eV) and Fe_2O_3 (1.4 eV), the valence band (VB) positions of TiO_2 and Fe_2O_3 are $+2.68$ and $+1.70$ V, respectively. Based on the above results and discussion, a reasonable photocatalytic mechanism of $\text{TiO}_2/\text{Fe}_2\text{O}_3$ nanocomposites is proposed (Scheme 2). The relative location of the E_F of TiO_2 and Fe_2O_3 is concluded that the E_F of Fe_2O_3 is lower

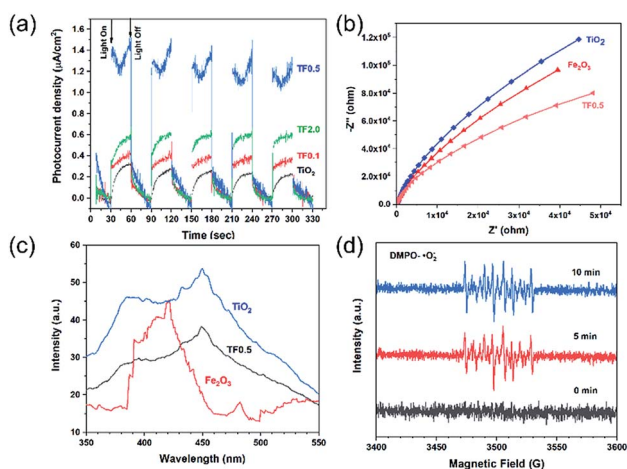
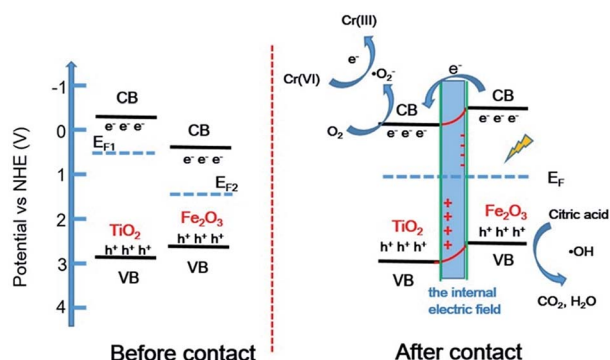


Fig. 8 (a) Photogenerated currents density curves, (b) EIS plots, (c) PL spectra of TiO_2 , TF0.5 and Fe_2O_3 , and (d) ESR signals of $\text{DMPO} \cdot \text{O}_2^-$ for TF0.5 irradiated for 0, 5 and 10 min by 300 W Xe lamp.



Scheme 2 Proposed photocatalytic mechanism diagram of $\text{TiO}_2/\text{Fe}_2\text{O}_3$ heterojunction photocatalysts.



than that of TiO_2 .^{2,3} When Fe_2O_3 contacts TiO_2 to form heterojunction, to acquire an equalized Fermi level, the electrons flow from TiO_2 to Fe_2O_3 resulting in a positive area forming in the heterojunction adjacent to TiO_2 ; whereas the holes flow from Fe_2O_3 to TiO_2 resulting in a negative area forming in the heterojunction adjacent to Fe_2O_3 . Meanwhile, an internal electric field directed from TiO_2 to Fe_2O_3 is constructed, which leads to the opposite direction of charge carries diffusion. Finally, the photogenerated electrons migrate from Fe_2O_3 to TiO_2 and holes migrate from TiO_2 to Fe_2O_3 under visible light irradiation. As a result of charge carries migration, electrons accumulate mainly on the CB of TiO_2 and then reduce dissolved oxygen molecules to yield superoxide radical ($\cdot\text{O}_2^-$), which leads to the photoreduction $\text{Cr}(\text{vi})$ on TiO_2 . In addition, ESR analyses (Fig. 8d) were used to further investigate the existence of $\cdot\text{O}_2^-$ species in the photocatalytic reaction systems of TF0.5. No obvious signal could be observed for TF0.5 in dark. However, six characteristic peaks of the DMPO- $\cdot\text{O}_2^-$ appeared in ESR curves of TF0.5 after 5 min irradiation. It can be concluded that photo-induced electron-hole pairs in TF0.5 has been effectively separated. Generally, $\text{Cr}(\text{vi})$ could be reduced by either photo-generated electrons (e^-) or $\cdot\text{O}_2^-$. The feasible reaction steps (1)–(9) in the photocatalytic process are as follows:^{55–57}

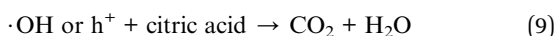
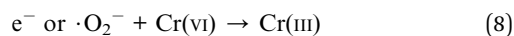
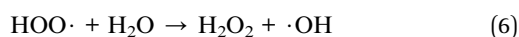
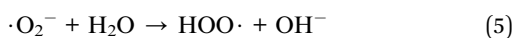
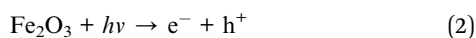
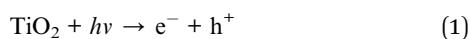


Fig. S6† shows the effect of citric acid on photoreduction $\text{Cr}(\text{vi})$ of TF0.5. Obviously, TF0.5 hardly reduces $\text{Cr}(\text{vi})$ without citric acid. Citric acid plays an important role in photocatalysis as it can capture holes (h^+) as a sacrificial reagent to restrain the recombination of electron-hole pairs.^{58,59} It is shown that the synergistic effect of the internal electric field at the heterojunction and citric acid promotes the separation of electron-hole pairs, enhancing the photocatalytic activity of the $\text{TiO}_2/\text{Fe}_2\text{O}_3$ nanocomposites.

Conclusions

In summary, we successfully prepared $\text{TiO}_2/\text{Fe}_2\text{O}_3$ nanocomposites by hydrothermal methods and deposited Fe_2O_3 on the surface of TiO_2 . The introduction of Fe_2O_3 enhanced the

visible light absorption of the composites. The construction of heterojunction structures and internal electric fields at the interface of the composites promotes the separation of electron-hole pairs, and citric acid consumes holes for restraining the recombination of electron-hole pairs. With the synergistic effect of these processes, the as-prepared photocatalysts performed high photocatalytic efficiency in the process of photo-reduction $\text{Cr}(\text{vi})$, for example, the efficiency of reducing $\text{Cr}(\text{vi})$ to $\text{Cr}(\text{iii})$ in TF0.5 reached 100% within 160 minutes.

Conflicts of interest

There are no conflicts to declare.

Acknowledgements

This research was financially supported by the National Natural Science Foundation of China (No. 21868036), the National Natural Science Foundation of Xinjiang Uyghur Autonomous Region (No. 2016D01C037) and the Project of Xinjiang Education Office (No. XJEDU20171004). We thank the Thousand Talents program. We thank the test platform in the Ministry Key Laboratory of Oil and Gas Fine Chemicals for assistance with the UV-vis spectroscopic measurement. The authors acknowledge facilities and staff at the Physical and Chemical Testing Centre of Xinjiang University.

Notes and references

- 1 K. Nakata, T. Ochiai, T. Murakami and A. Fujishima, *Electrochim. Acta*, 2012, **84**, 103–111.
- 2 W. J. Wang, G. Y. Li, D. H. Xia, T. C. An, H. J. Zhao and P. K. Wong, *Environ. Sci.: Nano*, 2017, **4**, 782–799.
- 3 H. Zhang, X. J. Lv, Y. M. Li, Y. Wang and J. H. Li, *ACS Nano*, 2010, **4**, 380–386.
- 4 B. Liu, A. Khare and E. S. Aydil, *ACS Appl. Mater. Interfaces*, 2011, **3**, 4444–4450.
- 5 A. Amarjargal, Z. Jiang, L. D. Tijing, C. H. Park, I. T. Im and C. S. Kim, *J. Alloys Compd.*, 2013, **580**, 143–147.
- 6 A. Banisharif, A. A. Khodadadi, Y. Mortazavi, A. Anaraki Firooz, J. Beheshtian, S. Agah and S. Menbari, *Appl. Catal., B*, 2015, **165**, 209–221.
- 7 S. Khanchandani, S. Kumar and A. K. Ganguli, *ACS Sustainable Chem. Eng.*, 2016, **4**, 1487–1499.
- 8 C. C. Wang, Y. Zhan and Z. Y. Wang, *ChemistrySelect*, 2018, **3**, 1713–1718.
- 9 Q. J. Xiang, J. G. Yu and M. Jaroniec, *J. Am. Chem. Soc.*, 2012, **134**, 6575–6578.
- 10 J. Li, M. Zhang, X. Li, Q. Y. Li and J. J. Yang, *Appl. Catal., B*, 2017, **212**, 106–114.
- 11 Y. Q. Cui, Q. L. Ma, X. Y. Deng, Q. Meng, X. W. Cheng, M. Z. Xie, X. L. Li, Q. F. Cheng and H. L. Liu, *Appl. Catal., B*, 2017, **206**, 136–145.
- 12 J. B. Cai, X. Q. Wu, S. X. Li and F. Y. Zheng, *ACS Sustainable Chem. Eng.*, 2016, **4**, 1581–1590.
- 13 J. Du, X. Y. Lai, N. L. Yang, J. Zhai, D. Kisailus, F. B. Su, D. Wang and L. Jiang, *ACS Nano*, 2011, **5**, 590–596.



- 14 X. B. Chen and A. Selloni, *Chem. Rev.*, 2014, **114**, 9281–9282.
- 15 J. Schneider, M. Matsuoka, M. Takeuchi, J. L. Zhang, Y. Horiuchi, M. Anpo and D. W. Bahnemann, *Chem. Rev.*, 2014, **114**, 9919–9986.
- 16 J. X. Low, J. G. Yu, M. Jaroniec, S. Wageh and A. A. Al-Ghamdi, *Adv. Mater.*, 2017, **29**, 1601694.
- 17 S. J. A. Moniz, S. A. Shevlin, D. J. Martin, Z.-X. Guo and J. Tang, *Energy Environ. Sci.*, 2015, **8**, 731–759.
- 18 H. Wang, L. Zhang, Z. Chen, J. Hu, S. Li, Z. Wang, J. Liu and X. Wang, *Chem. Soc. Rev.*, 2014, **43**, 5234–5244.
- 19 P. Li, X. Zhao, C. J. Jia, H. G. Sun, L. M. Sun, X. F. Cheng, L. Liu and W. L. Fan, *J. Mater. Chem. A*, 2013, **1**, 3421–3429.
- 20 M. Z. Xie, Q. Q. Meng, P. Luan, Y. J. Feng and L. Q. Jing, *RSC Adv.*, 2014, **4**, 52053–52059.
- 21 T. Wang, G. D. Yang, J. Liu, B. L. Yang, S. J. Ding, Z. F. Yan and T. C. Xiao, *Appl. Surf. Sci.*, 2014, **311**, 314–323.
- 22 M. X. Sun, Y. L. Fang, Y. Y. Kong, X. J. Yuan, J. F. Shi and A. Umar, *J. Alloys Compd.*, 2017, **705**, 89–97.
- 23 L. L. Peng, T. F. Xie, Y. C. Lu, H. M. Fan and D. J. Wang, *Phys. Chem. Chem. Phys.*, 2010, **12**, 8033–8041.
- 24 Z. Zhang and J. T. Yates, *Chem. Rev.*, 2012, **112**, 5520–5551.
- 25 H. G. Yang, G. Liu, S. Z. Qiao, C. H. Sun, Y. G. Jin, S. C. Smith, J. Zou, H. M. Cheng and G. Q. Lu, *J. Am. Chem. Soc.*, 2009, **131**, 4078–4083.
- 26 X. G. Han, Q. Kuang, M. S. Jin, Z. X. Xie and L. S. Zheng, *J. Am. Chem. Soc.*, 2009, **131**, 3152–3153.
- 27 P. W. Li, Z. Q. He, C. X. Luo, Y. Xiao, Y. Wang, J. Hu, G. Li, H. B. Jiang and W. D. Zhang, *Appl. Surf. Sci.*, 2019, **466**, 185–192.
- 28 T. Shi, Y. Y. Duan, K. L. Lv, Z. Hu, Q. Li, M. Li and X. F. Li, *Front. Chem.*, 2018, **6**, 175.
- 29 C. R. Hubbard and R. L. Snyder, *Powder Diffr.*, 1988, **3**, 74–77.
- 30 S. Hillier, *Clay Miner.*, 2000, **35**, 291–302.
- 31 D. Liu, Z. H. Li, W. Q. Wang, G. Q. Wang and D. Liu, *J. Alloys Compd.*, 2016, **654**, 491–497.
- 32 X. Cao, S. Q. Luo, C. Liu and J. W. Chen, *Adv. Powder Technol.*, 2017, **28**, 993–999.
- 33 O. Akhavan, *Appl. Surf. Sci.*, 2010, **257**, 1724–1728.
- 34 L. Liang, K. N. Li, K. L. Lv, W. K. Ho and Y. Y. Duan, *Chin. J. Catal.*, 2017, **38**, 2085–2093.
- 35 X. Zhao, Y. T. Du, C. J. Zhang, L. J. Tian, X. F. Li, K. J. Deng, L. Q. Chen, Y. Y. Duan and K. L. Lv, *Chin. J. Catal.*, 2018, **39**, 736–746.
- 36 S. M. Zhu, F. Yao, C. Yin, Y. Li, W. H. Peng, J. Ma and D. Zhang, *Microporous Mesoporous Mater.*, 2014, **190**, 10–16.
- 37 P. Zhang, L. Yu and X. W. Lou, *Angew. Chem., Int. Ed.*, 2018, **57**, 15076–15080.
- 38 A. A. Tahir, M. A. Ehsan, M. Mazhar, K. G. U. Wijayantha, M. Zeller and A. D. Hunter, *Chem. Mater.*, 2010, **22**, 5084–5092.
- 39 G. K. Mor, O. K. Varghese, M. Paulose and C. A. Grimes, *Adv. Funct. Mater.*, 2005, **15**, 1291–1296.
- 40 S. Mansingh, D. K. Padhi and K. M. Parida, *Catal. Sci. Technol.*, 2017, **7**, 2772–2781.
- 41 J. Tauc, R. Grigorovici and A. Vancu, *Phys. Status Solidi B*, 1966, **21**, 123–126.
- 42 B. D. Viezbicke, S. Patel, B. E. Davis and D. P. Birnie III, *Phys. Status Solidi B*, 2015, **252**, 1700–1710.
- 43 Y. Xu, W. Wen and J. M. Wu, *J. Hazard. Mater.*, 2018, **343**, 285–297.
- 44 X. B. Hou, S. L. Stanley, M. Zhao, J. Zhang, H. M. Zhou, Y. B. Cai, F. L. Huang and Q. F. Wei, *J. Alloys Compd.*, 2019, **777**, 982–990.
- 45 S. E. Chamberlin, I. H. Nayyar, T. C. Kaspar, P. V. Sushko and S. A. Chambers, *Appl. Phys. Lett.*, 2015, **106**, 1–5.
- 46 P. Mallick, *Mater. Sci.*, 2014, **32**, 193–197.
- 47 S. Kment, F. Riboni, S. Pausova, L. Wang, L. Y. Wang, H. Han, Z. Hubicka, J. Krysa, P. Schmuki and R. Zboril, *Chem. Soc. Rev.*, 2017, **46**, 3716–3769.
- 48 J. Krysa, A. Nemeckova, M. Zlamal, T. Kotrla, M. Baudys, S. Kment, Z. Hubicka and M. Neumann-Spallart, *J. Photochem. Photobiol., A*, 2018, **366**, 12–17.
- 49 S. J. Yuan, J. K. Mu, R. Y. Mao, Y. G. Li, Q. H. Zhang and H. Z. Wang, *ACS Appl. Mater. Interfaces*, 2014, **6**, 5719–5725.
- 50 W. Jiang, X. Zong, L. An, S. Hua, X. Miao, S. Luan, Y. Wen, F. F. Tao and Z. Sun, *ACS Catal.*, 2018, **8**, 2209–2217.
- 51 X. L. Xing, H. H. Zhu, M. Zhang, L. L. Hou, Q. Y. Li and J. J. Yang, *Catal. Sci. Technol.*, 2018, **8**, 3629–3637.
- 52 B. J. Sun, W. Zhou, H. Z. Li, L. P. Ren, P. Z. Qiao, F. Xiao, L. Wang, B. J. Jiang and H. G. Fu, *Appl. Catal., B*, 2018, **221**, 235–242.
- 53 A. Wolcott, W. A. Smith, T. R. Kuykendall, Y. P. Zhao and J. Z. Zhang, *Adv. Funct. Mater.*, 2009, **19**, 1849–1856.
- 54 L. Kavan, M. Graetzel, S. E. Gilbert, C. Klemenzt and H. J. Scheel, *J. Am. Chem. Soc.*, 1996, **118**, 6716–6723.
- 55 X. K. Zeng, Z. Y. Wang, N. Meng, D. T. McCarthy, A. Deletic, J. H. Pan and X. W. Zhang, *Appl. Catal., B*, 2017, **202**, 33–41.
- 56 W. Liu, J. R. Ni and X. C. Yin, *Water Res.*, 2014, **53**, 12–25.
- 57 M. A. Ahmed, E. E. El-Katori and Z. H. Gharni, *J. Alloys Compd.*, 2013, **553**, 19–29.
- 58 B. R. James and R. J. Bartlett, *J. Environ. Qual.*, 1983, **12**, 173–176.
- 59 L. X. Yang, Y. Xiao, S. H. Liu, Y. Li, Q. Y. Cai, S. L. Luo and G. M. Zeng, *Appl. Catal., B*, 2010, **94**, 142–149.

